Journal of Zhejiang University-SCIENCE A 2025 26(12):1244-1257
www.jzus.zju.edu.cn; www.springer.com/journal/11582
E-mail: jzus_a@zju.edu.cn

Research Article
https://doi.org/10.1631/jzus.A2400529

Check for updates

Aerodynamic characteristics and carbody dynamic stress analysis for high-speed trains passing through a tunnel under crosswinds

Beikun WANG, Yaohui LU✉, Da FENG, Chuan XIAN, Yueheng XIANYU

School of Mechanical Engineering, Southwest Jiaotong University, Chengdu 610031, China

Abstract: The structural safety of high-speed trains is significantly endangered by increasing operating speeds. The objective of this research was to investigate the evolution of the flow field in trains passing through a tunnel while there is a strong crosswind at the tunnel entrance and exit. Moreover, the effect of aerodynamic pressure waves on structural strength was analyzed to evaluate the safety of the carbody. In this study, we selected the improved delayed detached-eddy simulation (IDDES) method as a turbulence model. The mechanism of interaction among the train, tunnel, and crosswind was evaluated through a complex computational fluid dynamics (CFD) model, simulating high-speed trains moving through tunnels at various crosswind speeds. Additionally, the dynamic stress response of the carbody was calculated using a sequential coupling approach, where integral aerodynamic forces were applied as substitutes for direct CFD pressure loads. We assessed the effect of aerodynamic loads on the dynamic stresses of the carbody at different crosswind velocities (0, 10, 15, and 20 m/s). The results indicate that crosswinds exert a substantial influence on the fluid structure surrounding the train. Consequently, the aerodynamic forces contribute significantly to potential damage to the carbody, posing increased safety risks for high-speed trains.

Key words: High-speed train; Crosswind; Aerodynamic loads; Dynamic stress; Safety evaluation

1 Introduction

The expansion of high-speed trains (HSTs) into mountainous regions necessitates extensive tunnel networks to maintain operational efficiency. However, the aerodynamic challenges associated with tunnel transit, particularly under crosswind conditions, have emerged as critical barriers to ensuring structural safety and ride comfort (Deng et al., 2023; Zhou et al., 2023; Liu et al., 2024; Wang et al., 2024; Hu et al., 2025). When HSTs traverse tunnels at high speeds, transient pressure waves and turbulence intensify aerodynamic loads on the carbody (Baker, 2014). This phenomenon necessitates urgent investigation, as crosswinds further amplify these loads, creating complex, unsteady flow fields that could compromise structural integrity (Mohebbi et al., 2024). Studies confirm that tunnel exits under crosswinds induce dramatic fluctuations in aerodynamic pressure and velocity, significantly elevating mechanical stress on critical carbody components (Deng et al., 2020; Wang et al., 2022). Such interactions have been linked to structural fatigue and localized cracking, as observed in field reports (Liu et al., 2021; Niu et al., 2023). The specific damage site is shown in Section S1 of the electronic supplementary materials (ESM).

While prior research has advanced understanding of isolated aerodynamic or mechanical loads, critical knowledge gaps persist in quantifying their coupled effects. For instance, Liu et al. (2019) identified altered dynamic responses in tunnels but omitted crosswind-turbulence coupling. Similarly, Lu et al. (2019) highlighted the scarcity of transient aerodynamic load integration in fatigue assessments, yet their sequential coupling method lacked crosswind variability. Although Jing et al. (2019) advocated for transient load modeling, their zonal approach did not address crosswind-modified pressure wave propagation. Furthermore, bidirectional fluid–structure interaction (FSI) methods (Dou et al., 2019) remain computationally prohibitive for practical applications, while simplified unidirectional

✉ Yaohui LU, yhlu2000@swjtu.edu.cn
Beikun WANG, https://orcid.org/0009-0005-7806-9002
Yaohui LU, https://orcid.org/0000-0002-5104-4842

Received Nov. 13, 2024; Revision accepted May 6, 2025;
Crosschecked Oct. 21, 2025; Online first Dec. 11, 2025

© Zhejiang University Press 2025

models fail to capture crosswind-induced flow asymmetries (Cui and Zhang, 2011). Crucially, no study has systematically resolved the interplay between aerodynamic excitation, tunnel pressure dynamics, and track-induced vibrations. The multi-source coupling mechanism is the main determinant of structural strength.

In this study, we established a complex computational fluid dynamics (CFD) model to examine train–tunnel–crosswind interactions by simulating high-speed trains moving through tunnels at various crosswind speeds. Using a sequential coupling approach, integral aerodynamic forces replace direct CFD pressure loads to compute the carbody's dynamic stress response under crosswinds of 0, 10, 15, and 20 m/s, thereby exploring aerodynamic load contributions to carbody dynamic stresses across variable crosswind intensities.

The structure of this paper is organized as follows: Section 2 presents the methodology for the CFD and finite element analysis (FEA), and introduces the establishment of the aerodynamic model and carbody finite element (FE) model. Section 3 reveals the distribution of aerodynamic loads on the carbody surface, and the dynamic response of the carbody is also analyzed for different side wind conditions. Finally, Section 4 provides a summary and a short discussion of this study.

2 Numerical simulation details

2.1 CFD simulation

2.1.1 Numerical method

In compressible inflow scenarios characterized by Mach numbers exceeding 0.3, coupled with complex aerodynamic phenomena observed in HSTs operating under crosswind conditions and tunnel environments, turbulence and unsteady behavior are consistently observed within the flow field. To ensure computational accuracy, the selection of an appropriate turbulence model is deemed essential. The shear stress transport (SST) k-ω model is widely used due to its demonstrated capability in resolving flow separation phenomena (Wang et al., 2021). However, the Reynolds-averaged Navier-Stokes (RANS) approach is recognized to preclude the capture of transient flow features and vortex dynamics due to its inherent averaging of fluctuating components. While large eddy simulation (LES) has been shown to enable the resolution of instantaneous flow structures, significant computational resources are required for its implementation. The detached eddy simulation (DES) methodology, formulated through the integration of RANS and LES advantages, enables the resolution of transient large-scale vortex evolution within practical computational constraints. Nevertheless, the predictive accuracy of this approach was found to be critically dependent on near-wall mesh resolution characteristics. The improved delayed detached-eddy simulation (IDDES) was developed as an advanced hybrid numerical methodology, in which core methodologies from delayed detached-eddy simulation (DDES) and wall-modeled large eddy simulation (WMLES) are synergistically integrated. Notable advantages were shown in the mitigation of modeled-stress depletion (MSD) and grid-induced separation (GIS) phenomena, accompanied by a significant reduction in Reynolds number dependency within near-wall flow regimes while physical consistency was preserved. A computational framework incorporating the IDDES approach with the SST k-ω turbulence model was subsequently established. This modeling paradigm has been extensively validated in rail transit aerodynamics research, with successful implementation documented in vortex characterization studies spanning diverse HST configurations (Deng et al., 2023; Wang et al., 2024). The specific equations of the IDDES turbulence model are presented in Section S2 of the ESM.

2.1.2 Computational model and boundary conditions

The HST surface was assumed to be aerodynamically smooth, with geometric details of door handles, pantographs, and suspension equipment being systematically neglected. A three-car model incorporating bogie assemblies, windscreen profiles, and wiper geometries was developed with dimensional accuracy to represent the operational HST configuration. This truncated configuration was selected in preference to the full eight-car arrangement based on the aerodynamic stability observed in the middle sections of conventional HSTs, where consistent cross-sectional profiles are maintained. The characteristic vertical dimension was standardized at H=4.05 m. A simplified geometric representation and corresponding dimensional parameters are presented in Fig. 1.

The numerical domain was rigorously constructed in compliance with BS EN 14067-6 standards (CEN,

2018), featuring an obstruction ratio of 0.112 and geometric parameters detailed in Fig. 2.

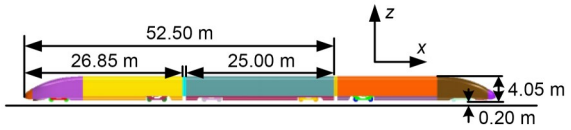

Fig. 1 Geometric model of the HST

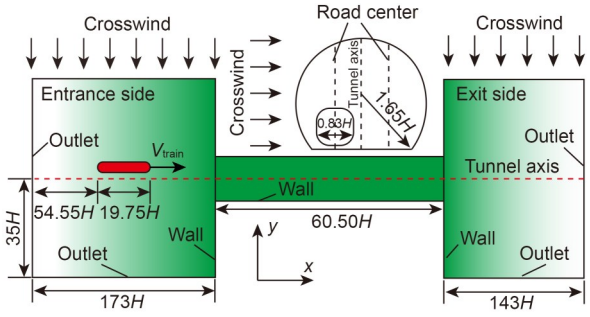

Fig. 2 Computational domains and boundary conditions

This schematic employs a top-down perspective to facilitate the visual representation of a train's movement along the x-axis within a tunnel environment, where V_{train} denotes both the train's direction of travel and its operating speed. A straight tunnel configuration with 60.5H length was implemented, positioned 98.7H downstream from the train nose initialization point. Simultaneously, by establishing extended open areas upstream of the tunnel at 173H and downstream at 143H, with a width of 70H and height of 35H, the stability of boundary conditions is ensured. The HST operated at 400 km/h under four crosswind scenarios (0, 10, 15, and 20 m/s), selected through synthesis of the China Railway Corporation regulatory guidelines and contemporary aerodynamic research (CR, 2014; Niu et al., 2022; Wang et al., 2022). The HST surface and the ground are bounded by no-slip walls, the crosswind inlet is bounded by a uniform wind velocity inlet boundary condition, and the remaining boundaries are pressure far-field.

2.1.3 Grid generation and solution process

Previous studies have extensively used overset grid methods to simulate object motion, as demonstrated by Zhou et al. (2019). Overset meshes are particularly advantageous for modeling intricate, winding flows around complex shapes and for scenarios involving multiple objects moving in opposite directions. Additionally, there have been successful implementations of these methods in parallel computing environments. In this study, regions experiencing substantial flow field variations—such as the bogie area, carbody flow region, and windscreen—were individually refined with an enhanced surface mesh size of 0.012 m. The overset mesh technique was applied to simulate the motion of the train, with the overset and background regions arranged as depicted in Fig. 3a.

The initial boundary layer mesh size (h_0) was set to 0.25 mm, with a growth rate of 1.2. Considering the computational model in this study is a full-scale HST with complex 3D external flow characteristics, the total grid count is exceptionally large. To control the grid quantity while referencing the methodologies of numerous scholars (Liu et al., 2020), standard wall functions were used for near-wall turbulence treatment. By setting the first-layer grid height at the wall boundary to maintain y^+ values of about 30, the accuracy of standard wall functions in turbulent boundary layer simulations was ensured. As shown in Fig. 3b, the average y^+ distribution on the train surface was about 30, which is similar to the results obtained by Liu et al. (2020). Due to crosswind effects, the gradient of flow field variables on the leeside of the train was notably high, necessitating further mesh refinement in designated regions (Region B) with a grid size of 0.12 m. The overall computational model, in its final configuration, included no fewer than 37.39 million grid cells. In this paper, the control equations are discretized into algebraic equations using the finite volume method. The semi-implicit method for pressure-linked equations (SIMPLE) algorithm is used to perform the pressure–velocity interaction. Second-order implicit format discrete-time terms are used for unsteady flow calculations. The momentum and turbulence equations are solved using an algebraic multigrid (AMG) linear solver (Wang and Xu, 2023). The Courant number (Co) is chosen based on the actual physical properties reflected, and the Co is taken to be about 1 to satisfy interpolation precision of the overset mesh, so that the distance travelled by the train at each time step is one grid length. The mesh size at the junction of the overlapping grid and the background grid is 0.12 m. The time step is calculated from Eq. (1) to be 0.001 s, similar to the time step adopted in previous studies (Wang et al., 2021). The residuals of the continuity, momentum, and turbulence

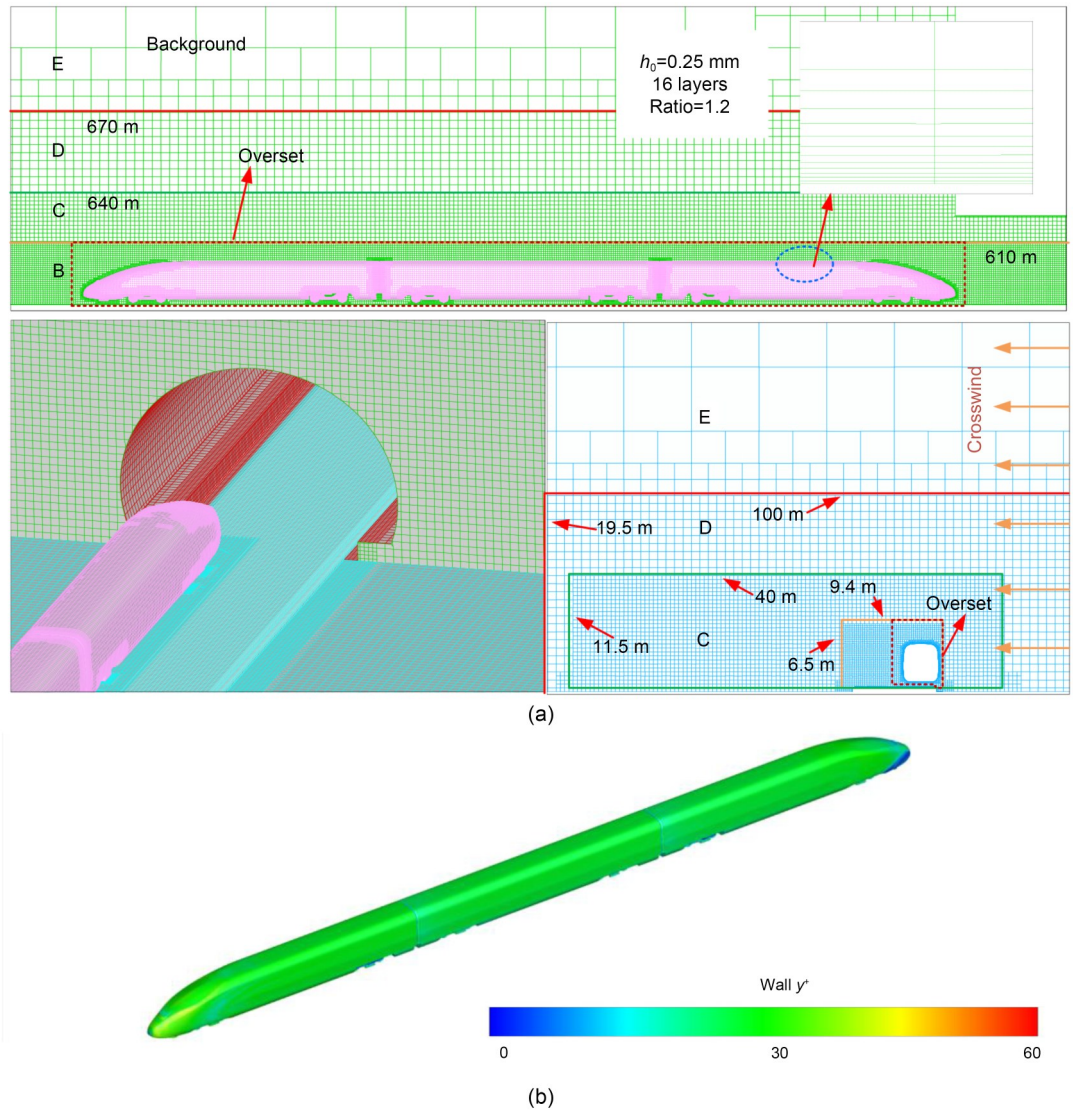

Fig. 3 Computational domain mesh setting and wall y^+ distribution: (a) grids of computational domain and boundary layers; (b) wall y^+ distribution of the train. References to color refer to the online version of this figure

equations are all less than 10^{-5} with 20 iterations per time step, and the Courant number Co can be formulated as follows:

$$Co=\frac{U\Delta t}{\mathrm{d}x}, \tag{1}$$

where Δt is the time step, dx is the length of the grid in the overset region, and U is the velocity with respect to the grid.

2.1.4 CFD verification: grid independence and experimental validation

To verify the accuracy of the numerical results provided in this study and validate the appropriateness of the turbulence model selection, we referenced wind tunnel test results conducted by Xia et al. (2017) at the Shanghai Automotive Wind Tunnel Center (SAWTC), China. This wind tunnel test was carried out using a 1:8-scale train model with a maximum speed of 250 km/h, turbulence intensity of less than 0.5%, and a test Reynolds number ranging from 7.5×10^5 to 1.9×10^6. The geometry of the numerical model described in this paper is the same as that of the wind tunnel tests. To eliminate the influence of grid resolution on calculation accuracy, the mesh density and the numerical algorithm are set as in Section 2.1.3. The scaled model height is defined as the characteristic length D (Fig. 4a). In Figs. 4b and 4c, EXP denotes experimental data for

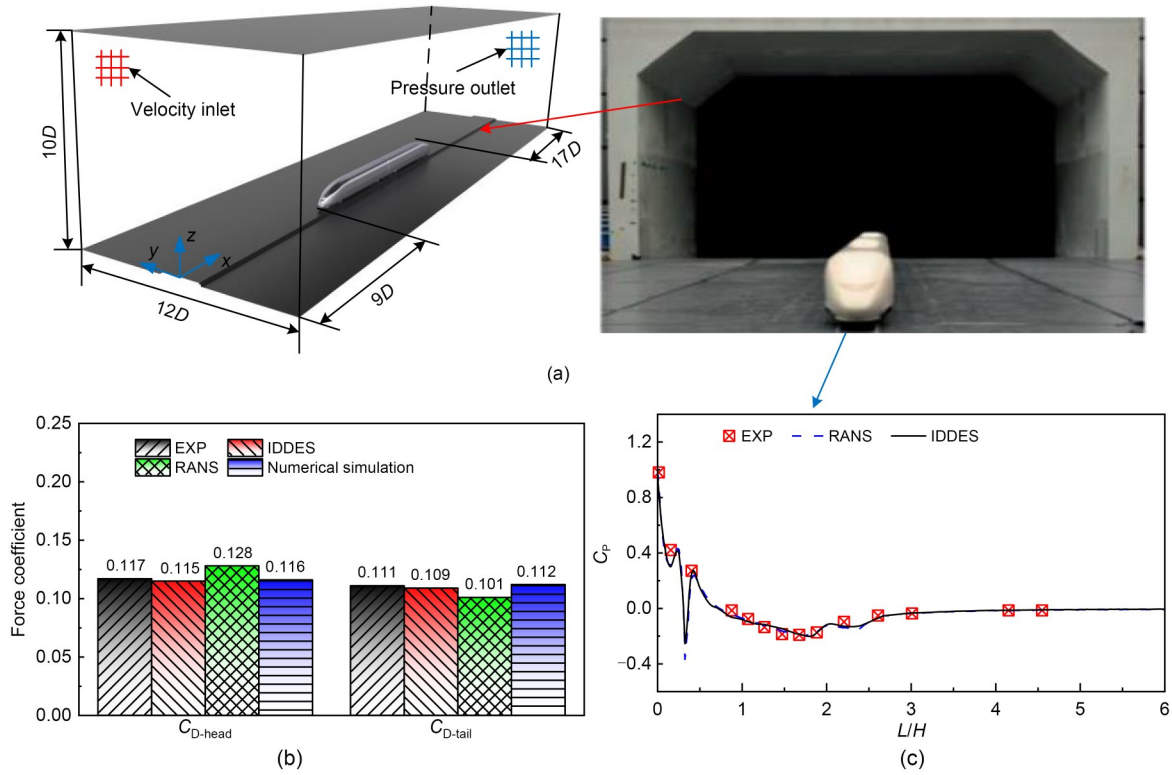

Fig. 4 Comparison of data from CFD numerical simulation and wind tunnel tests: (a) wind tunnel test diagram and computational domain configuration for numerical simulation verification; (b) comparison of drag coefficients for leading and trailing vehicles predicted by different turbulence models against wind tunnel test results; (c) comparison of pressure distribution on streamlined vehicle front ends. References to color refer to the online version of this figure

the train, $C_{D\text{-head}}$ represents the head car drag coefficient, $C_{D\text{-tail}}$ denotes the tail car drag coefficient, C_p denotes the surface pressure coefficient, and L denotes the train length. A comprehensive comparison was conducted between the pressure distributions across the streamlined nose section predicted by various turbulence models and the drag coefficients of both the head car and tail car, benchmarked against wind tunnel test results. The comparative analysis revealed that the implementation of the IDDES turbulence model showed superior predictive accuracy in capturing both pressure gradients and aerodynamic drag characteristics.

To verify the grid independence, the time-statistical averaging results of the aerodynamic force of the head car before entering the tunnel at a crosswind speed of 15 m/s were compared for four different grid numbers. The differences among the four grids are shown in Table 1, where Δz is the thickness of the first layer of the mesh and Δn is the size of the HST surface mesh. When an HST operates under a crosswind, it will be subjected to fluid drag, lift, and lateral forces. The drag coefficient C_D, lift coefficient C_L, and lateral force coefficient C_S in this study are shown in Eq. (2). After the operation is stabilized, data selection is carried out, as detailed in Section S3 of the ESM.

$$\begin{cases} C_D = \dfrac{F_D}{0.5\rho U_m^2 S}, \\ C_L = \dfrac{F_L}{0.5\rho U_m^2 S}, \\ C_S = \dfrac{F_S}{0.5\rho U_m^2 S}, \end{cases} \tag{2}$$

where F_D is the drag force, F_L is the lift force, F_S is the lateral force, the air density parameter ρ is equal to 1.225 kg/m^3, U_m is the freestream velocity, and S is the maximum cross-sectional area of the HST.

The number of grids is controlled by controlling the range of y^+. The error is the aerodynamic difference between neighbouring grid densities. Table 1 shows that the results for G-0 and G-1 deviate significantly from the others. The error represents the discrepancy between the results of two adjacent dense grids and

Table 1 Grid convergence study

Item	Δz (mm)	Δn (m)	Total grid number (million)	C_D	Error of C_D (%)	C_L	Error of C_L (%)	C_S	Error of C_S (%)
G-0	0.31	0.022	18.54	0.179	–	0.236	–	0.644	–
G-1	0.28	0.017	26.32	0.169	5.9	0.223	5.8	0.601	7.1
G-2	0.25	0.012	37.39	0.163	3.6	0.227	1.7	0.580	3.6
G-3	0.22	0.010	41.13	0.159	2.5	0.229	0.8	0.591	1.8
Ref	–	–	–	0.158	–	0.231	–	0.587	–

sparse grids. The results of the other grids are very close, and G-2 was finally chosen to discretize the model, considering the computational accuracy and resources. In the table, Ref denotes the findings from another study (Tang et al., 2024). Comparing these results with the G-2 result reveals that the error margin is less than 5%.

To validate the robustness of the algorithm and settings used in this study, a comparative analysis was conducted using dynamic model test data from Miyachi et al. (2016). The details are given in Section S4 of the ESM.

2.2 Dynamic stress simulation of the carbody

2.2.1 Numerical setup of the FE model of the carbody

In this study, an HST body with a length of 25 m and a width of 3.4 m was selected as the research subject. Constructed from large aluminum alloy hollow extrusion profiles, the HST body is designed without a longitudinal center beam or cross beams in the underframe. Due to the thin plate thicknesses of the body profiles and load-bearing structures relative to the body's longitudinal and transverse dimensions, stresses from mutual extrusion along the thickness direction can be neglected.

The FE model of the carbody incorporates both structural and stress characteristics, given the complex loading conditions encountered during operation, including vertical bending, transverse aerodynamic forces, longitudinal tension, and compression. To accurately represent these multi-axial loads, plate and shell elements are used, as they meet the engineering requirements for strength calculation (Lu et al., 2019). The FE model comprises 1166926 cells and 1087587 nodes, with plate thicknesses defined by cell-specific constants. Mass is represented by 0D elements, while 1D spring elements model the air springs. The stiffness of the plate-shell model closely aligns with that of the solid structure, ensuring fidelity in the FE model (Fig. 5). Section S5 of the ESM gives the content of the irrelevance verification of the finite element mesh.

The mechanical properties of aluminum alloys for an HST body are shown in Table 2. Aluminum alloy materials, which can be strengthened through heat treatment, exhibit moderate strength along with excellent weldability and corrosion resistance. They also show excellent performance in extrusion and pressure quenching, and can be used to produce large structures with complex shapes.

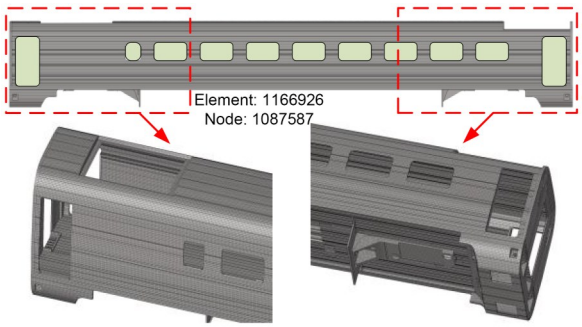

Fig. 5 FE model setup of the carbody. References to color refer to the online version of this figure

Table 2 Setting of the material properties of the carbody

Performance parameter	Value	
	6082-T6 alloy	5083 alloy
Density (kg/m^3)	2710	2660
Elastic modulus (MPa)	710000	703000
Poisson's ratio	0.33	0.33
Tensile strength (MPa)	279	270
Yield strength (MPa)	260	200

In this numerical simulation, key components such as the air conditioner, pantograph, transformer, auxiliary converter, and brake control box are incorporated in accordance with railway standard EN 12663-1 (CEN, 2010). These components are modeled as centralized mass points using couplings, while the suspension equipment is connected via multi-point constraints (MPCs). Passengers and seats are represented

as uniformly distributed mass points. Based on these considerations, the total mass of the carbody is calculated to be 46.45 t, as shown in Eq. (3):

$$F_{SV}=(m_1+nm_p+sm_b)g, \tag{3}$$

where F_{SV} denotes the vertical distributed load in the operation state, m_1 is the unload mass of the vehicle in kg, n is the number of passengers, m_p is the mass of each passenger, assumed to be 80 kg, s is the area of the luggage cabinet in m^2, m_b is the mass of luggage per unit area of the luggage cabinet, assumed to be 300 kg, and g is the acceleration due to gravity, taken as 9.81 m/s^2.

To accurately simulate actual operating conditions, it is essential to combine aerodynamic loads with vertically distributed loads, which are uniformly applied to the chassis. Mechanical loads are introduced at the positions of the four air springs, while also taking into account the dead weight of the body. The green area in Fig. 5 shows that the body glass receives aerodynamic loads. These are treated by adding coupling points in the center of the window to couple the aerodynamic loads at the window.

The coupled load application methodology is illustrated in Fig. 6 and is based on the vehicle system dynamics model established by Wang et al. (2025). Real track irregularity data measured in China (Zheng et al., 2024) were used as excitation input to the dynamic model. This enabled the calculation of loads acting on the air springs during straight-section travel. The computed loads were then applied to the finite element model. The resulting mechanical load data are given in Section S6 of the ESM.

2.2.2 Method of aerodynamic loading

The difference in mesh scale between the FEA model and the CFD model of the carbody is significant, and the direct flow-solid coupling is difficult. In this study, we investigated the impact of aerodynamic forces on the dynamic stresses of the carbody, while the effect of elastic deformation on the flow field structure was out of scope. Previous studies (Jing et al., 2019; Lu et al., 2019) applied aerodynamic pressure

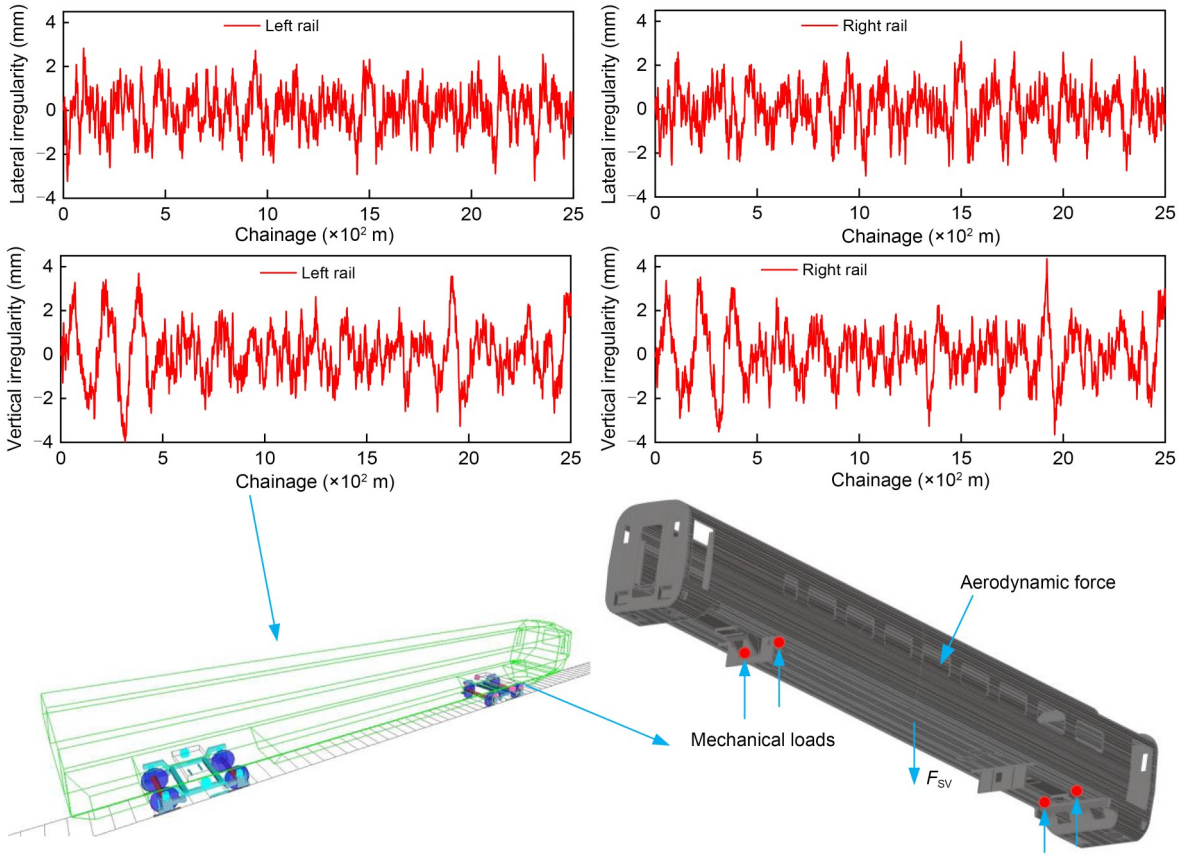

Fig. 6 Coupled loading method

waves to the carbody by sweeping, assuming that in the carbody's longitudinal region, pressure waves propagate sequentially with only a time lag between regions. However, as shown in Section S7 of the ESM, the pressure distribution on the longitudinal face of the carbody is different due to vortex interactions. Therefore, the above method is not able to characterize the effect of longitudinal pressure distribution on a vehicle body structure when subjected to crosswinds. Building on prior research, in this paper, we introduce a pneumatic load application method tailored to assess dynamic stresses on the carbody under crosswind conditions (Fig. 7), based on the principles of flow-solid coupling data transfer. The specific pneumatic load loading process is described in Section S8 of the ESM.

3 Results and discussion

3.1 Analysis of the train–tunnel–crosswind interaction mechanism

Section S7 of the ESM gives the location of the measurement points on the surface of the carbody and the results of the pressure wave at different measurement points on the carbody. The pressure waves do not affect the surface of the train simultaneously and have distinct longitudinal propagation characteristics. The differences between the upwind, leeward, and upper surfaces are large, but there are smaller differences between adjacent measurement points. The aerodynamic load on the train shows greater variation after exiting the tunnel than when entering. This result is consistent with the findings of other researchers (Liu et al., 2019). The measurement points are arranged inside the tunnel, with some shown in Fig. 8. All measurement points are 2.2 m above the track.

Fig. 9a shows sensors d_3/D_3 (windward) and e_3/E_3 (leeward) at the tunnel entrance. Windward peak pressure (d_3) decreases with crosswind velocity. Leeward pressure (e_3) increases significantly. At the exit (Fig. 9b), windward pressure fluctuates slightly. Leeward variations dominate, showing crosswind-driven flow changes. Fig. 9c reveals large leeward pressure oscillations 10 m upstream of the entrance. This indicates crosswind-induced flow disturbances during train ingress. Similarly, Fig. 9d shows amplified leeward

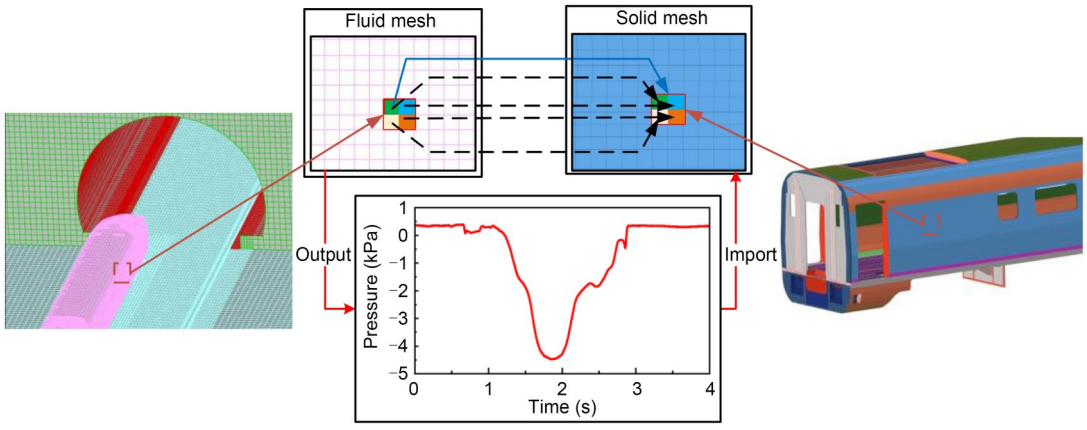

Fig. 7 Aerodynamic load transmission methods

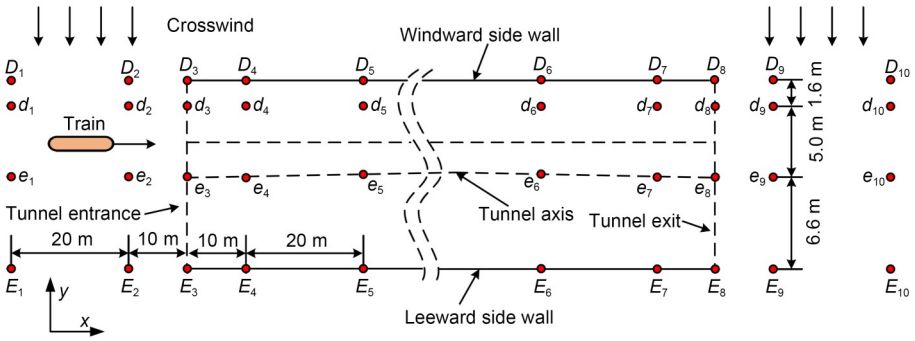

Fig. 8 Measurement points outside the tunnel

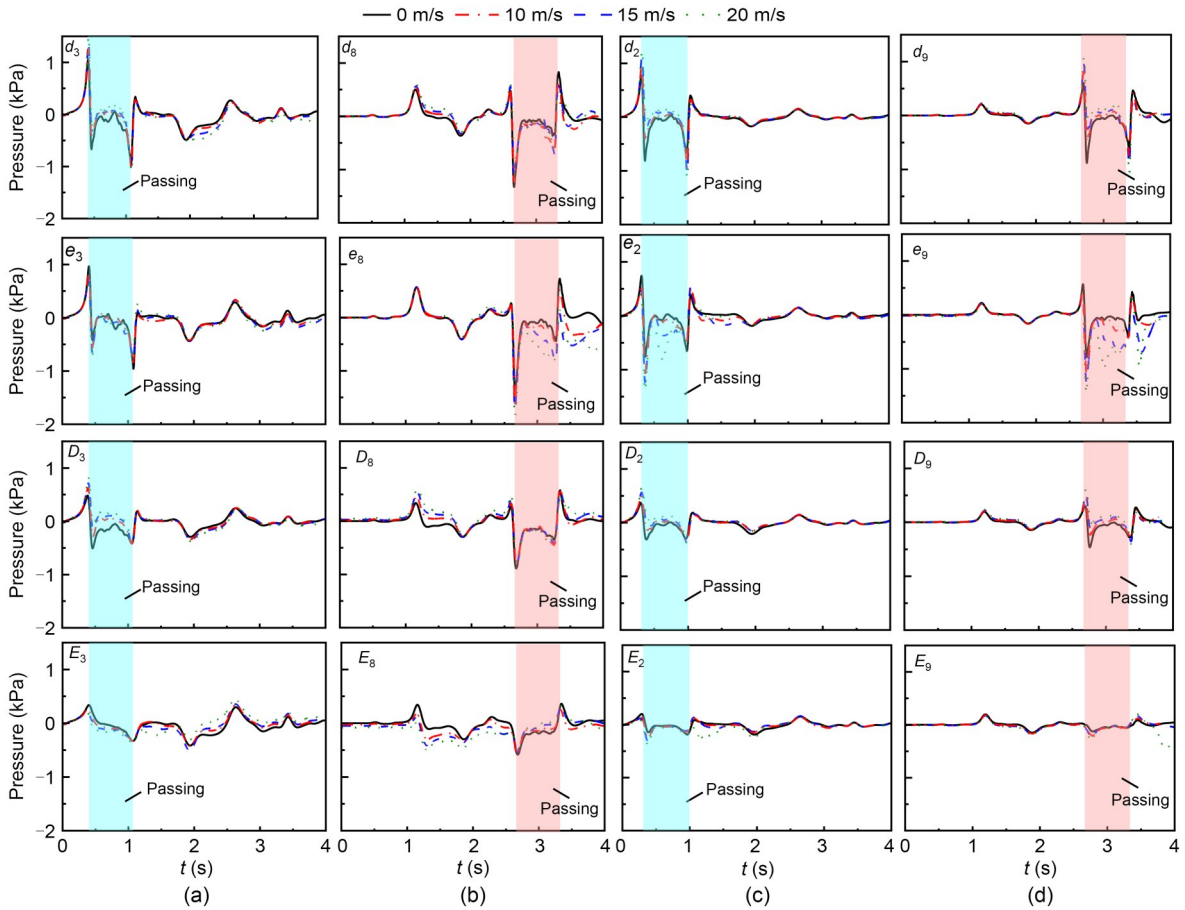

Fig. 9 Pressure variation curves at measurement points around the tunnel entrance and exit: (a) tunnel entrance; (b) tunnel exit; (c) 10 m before the tunnel entrance; (d) 10 m after the tunnel exit

fluctuations 10 m downstream of the exit. These scale with crosswind intensity. Crosswind is a critical driver of unsteady aerodynamic forces. It significantly alters flow structures during tunnel entry/exit. The flow structures at measurement points 1, 6, and 11 were analyzed during two critical phases: when the leading car enters the tunnel entrance and when the trailing car exits. The positions of the measuring points are derived from Section S7 of the ESM. Measurement point 1 aligns with section S_1; point 6 with S_2; point 11 with S_3 (Fig. 10). Pressure distributions across S_1–S_3 (Fig. 10a) show maximum negative pressure occurs at the upper windward corner. Airflow separation occurs on the leeward side under crosswinds. Vortex V_1 forms upstream and expands downstream. Vortex V_2 develops near the leeward ground. Vortex V_2 results from interactions with the track and terrain. During tunnel exit (Fig. 10b), the increasing distances Δx_2 and Δx_3 between vortex V_1 and the train lead to V_2 dissipation and altered V_3 dynamics. Crosswind-induced transverse vortices (V_1, V_2, V_3, and smaller-scale structures) emerge leeward as the train exits the tunnel. These vortices shed backwards and interact, with their morphology and trajectory modulated by tunnel and carbody obstructions.

Post-exit, transverse vortices undergo mutual interference, backward shedding, and tunnel-induced redirection, shifting toward the windward side near the portal. Notably, vortices remain unobstructed prior to tunnel entry. Pressure wave fluctuations arise mainly from flow field alterations driven by train–tunnel–crosswind coupling. Section S9 of the ESM describes the structure of the transient flow field as the train leaves the tunnel. The pressure wave dynamics originate mainly from changes in the flow field driven by the train–tunnel–crosswind coupling mechanism.

The power spectral density (PSD) of the pressure waves of the intermediate train is shown in Fig. 11. Frequencies (f) in the range of 0.5–4.0 Hz can cause trains to be more likely to vibrate.

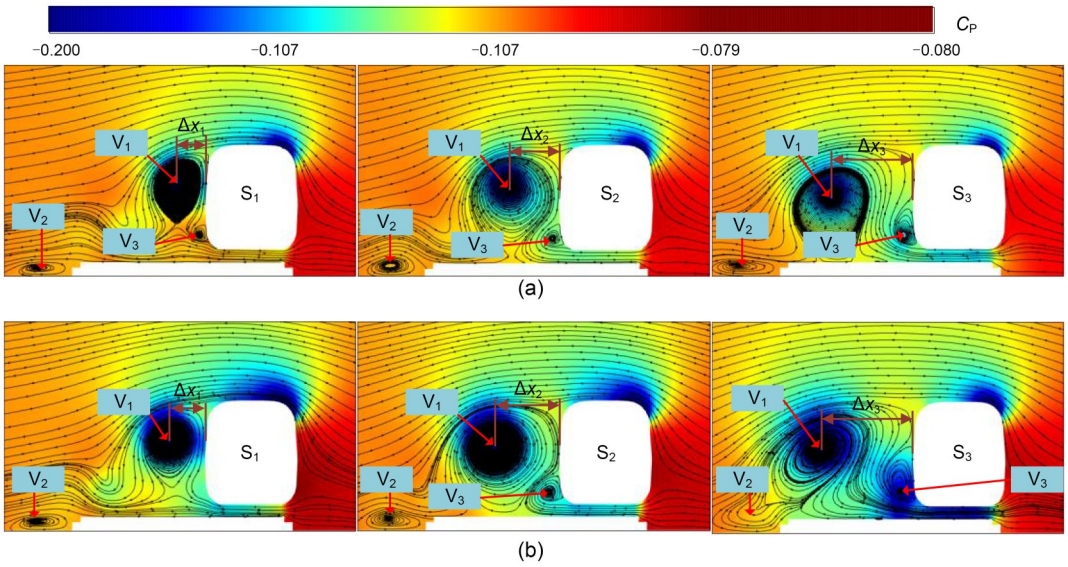

Fig. 10 Flow field structure in different sections of the intermediate car: (a) at the moment the train enters; (b) at the moment the train leaves. References to color refer to the online version of this figure

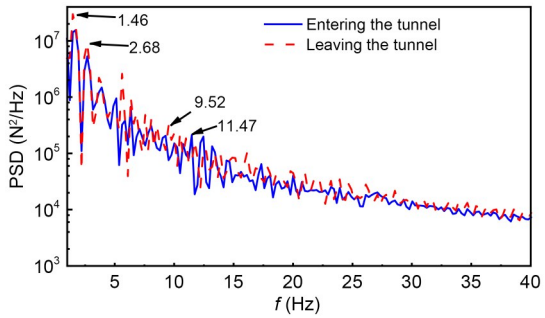

Fig. 11 Power spectral density of pressure waves on a train entering and leaving the tunnel

For the condition when the HST leaves the tunnel, the peaks of PSD are at f=1.46 and 2.68 Hz. They are both larger than when the HST enters the tunnel. In the range of 8–15 Hz, the frequency is close to the intrinsic frequency of the train, and the carbody structure is prone to elastic vibration. The maximum PSD value of the train leaving the tunnel corresponds to a frequency (9.52 Hz) closer to the intrinsic frequency of the train (NRA, 2019).

3.2 Contribution of the aerodynamic load to the structural stress of the carbody

In this study, the modal superposition method was used to simulate the dynamic response of the carbody under five working conditions. The five cases were as follows: Case 1 was to apply only mechanical loads, and Cases 2–5 were to apply aerodynamic loads corresponding to wind speeds of 0, 10, 15, and 20 m/s, respectively.

The scattering of carbody stress at different moments for Case 1 and Case 2 is presented in Fig. 12. Given the relatively minor variation in mechanical load, the dynamic stress distribution in the carbody is limited; thus, the stress distribution at t=1.8 s is provided for Case 1. It is evident that stresses near the windows at both ends of the sidewalls are significantly higher, while those near the central windows are comparatively lower. Upon entering the tunnel, the negative pressure on the carbody surface increases rapidly due to the "piston effect" of the tunnel, which elevates the aerodynamic load on the carbody's strength. At t=1.8 s, the stress in Case 2 is notably greater than in Case 1, particularly around the corners of the windows.

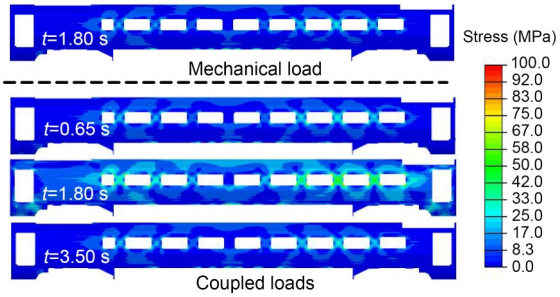

Fig. 12 Stress distribution in the carbody under different operating conditions. References to color refer to the online version of this figure

In accordance with the principle of stress concentration, five points of interest were selected (Fig. 13) based on the component connection parts that represent the load application locations, as well as the distribution depicted in the stress cloud map. Subsequently, the dynamic responses of the five points (M_1–M_5) of interest were calculated and analyzed.

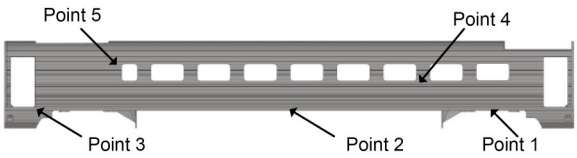

Fig. 13 Location of carbody points of interest

Fig. 14 illustrates the variation in stress at the carbody points of interest under different working conditions. For points M_2–M_5, the stress trends are generally consistent. Notably, the stresses under coupled loads are higher than those under mechanical loads, with mean stress values increasing as crosswind speed rises. However, at the moment of tunnel entry, the stresses under coupled loads decrease, falling below those from mechanical loads. Stress levels peak within the tunnel, and the amplitudes of stress fluctuations at the points of interest after exiting the tunnel are greater than those during entry. Variations in stress among the points of interest are reflected mainly in the mean values and magnitudes of fluctuating stresses outside the tunnel, as well as the maximum peak values inside. Differences between the points of interest within the tunnel under coupled loading conditions are minimal.

Dynamic stress is an integral parameter in the strength analysis and safety evaluation of HSTs. In this paper, we propose an index to represent the contribution of aerodynamic forces to the dynamic stresses in the carbody. The aerodynamic contribution rate (η) is defined in Eq. (4) as:

$$\eta = \frac{\sigma_{\text{total}} - \sigma_{\text{m}}}{\sigma_{\text{total}}}, \tag{4}$$

where σ_{m} is the maximum stress at each monitoring point on the carbody under mechanical loading, and σ_{total} is the maximum stress at each monitoring point under coupled mechanical and pneumatic loading. Section S10 of the ESM shows the maximum isoefficacy data for the three points of interest (M_3–M_5) for different time periods (before the tunnel, out of the tunnel, and in the tunnel).

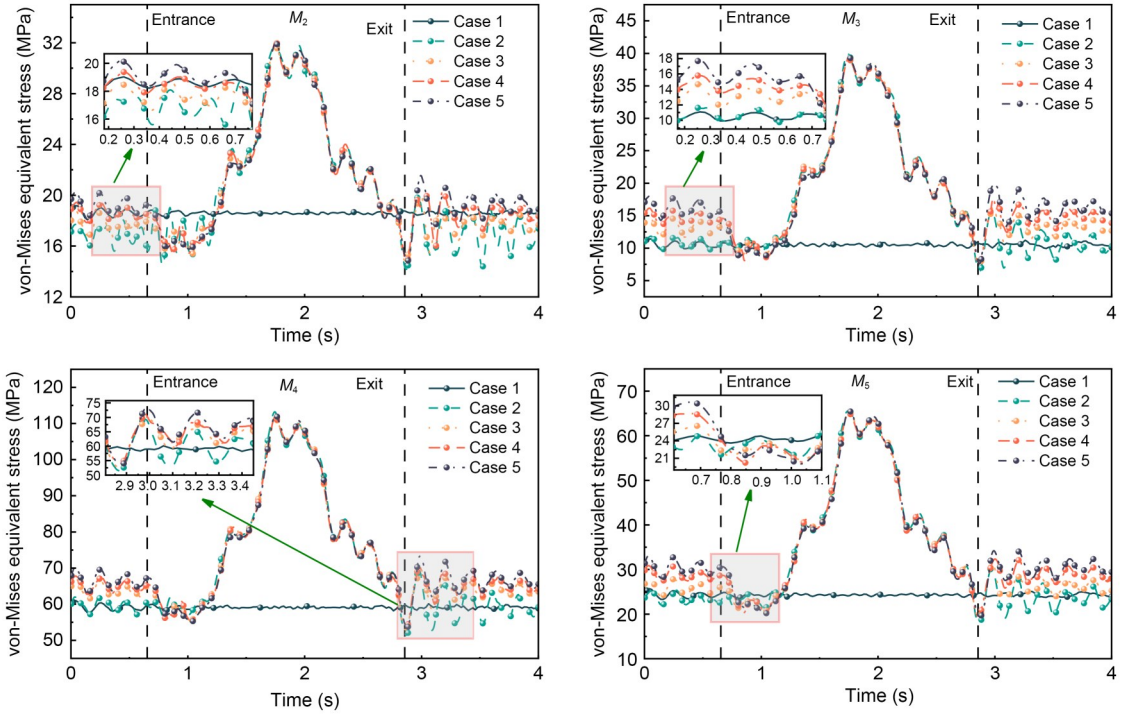

Fig. 14 Time course of stress at the points of interest under different working conditions. References to color refer to the online version of this figure

Fig. 15 shows η increasing with crosswind speed at all attention points. Inside the tunnel, η is very large (aerodynamic force dominant), but unaffected by crosswind speed. Before entering the tunnel, Case 5 increases the η of the three concerns by 33.6%, 11.5%, and 21.6%, respectively, compared to Case 2. Similarly, after exiting the tunnel, η increases by 15.1%, 4.6%, and 9.3%, respectively. For Case 2, leaving versus entering, η increases by 26.7%, 11.8%, and 16.9%. Equivalent force data (magnitude and mean) entering/leaving under different crosswinds are in Section S11 of the ESM. Dynamic stress amplitude is significantly higher near the exit than near the entrance across all crosswind conditions. Monitoring point M_4 shows the most pronounced crosswind effects. At location M_4, the mean stress increased by 0.6–67.0 MPa after exiting the tunnel, creating a critical fatigue zone under combined high static and intense dynamic loading.

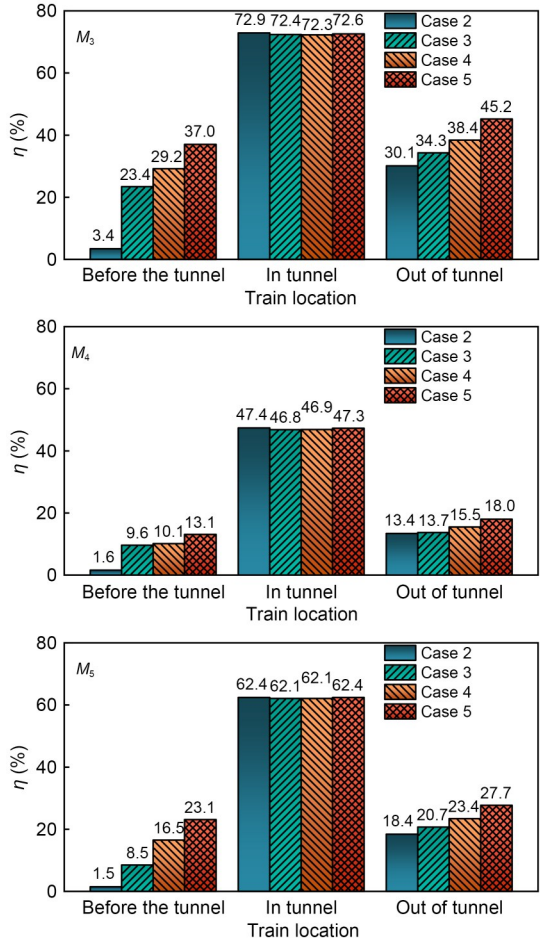

Fig. 15 Dynamic stresses on the carbody caused by aerodynamic loads as the train travels through the tunnel in various crosswinds

Meanwhile, both the dynamic stress amplitude and mean stress at the tunnel entrance progressively increased with stronger crosswinds, demonstrating cumulative structural loading from sustained wind action. To mitigate fatigue risks, implement localized stiffness reinforcement at M_4. Future studies should apply Goodman correction models to assess perimeter fatigue performance under operational conditions, clarifying wind–structure interaction mechanisms.

4 Conclusions

A complex CFD model was established to research the mechanism of train–tunnel–crosswind interaction and the characteristics of the flow field structure. Furthermore, the contribution of aerodynamic pressure to the dynamic stress response was investigated under different crosswind conditions. Our main conclusions are as follows:

The crosswind–tunnel coupling effect induces asymmetric vortex shedding. At the tunnel exit, compared to scenarios without crosswind conditions, transverse vortices generated by crosswinds increase the pressure fluctuation amplitudes on the leeward side. These vortices create localized low-pressure zones around the train, amplifying dynamic stress concentrations at window corners. Concurrently, as wind speed increases, the vibration response of the train shows a sustained increase. The aerodynamic load variation during the vehicle's exit from the tunnel under crosswind conditions significantly impacts the structural vibration response.

Spectral analysis identified two critical frequencies: 1.46 Hz (piston effect) and 9.52 Hz (vortex shedding), with the latter closely matching the bending mode of the carbody. This frequency coupling results in an increased stress amplitude on the sidewalls during the tunnel exit phase compared to the entry phase. Such resonance effects amplify stress responses, thereby increasing the likelihood of structural fatigue and long-term degradation, particularly at critical connection points such as window frames and joints. These findings suggest that unsteady aerodynamic loads must be fully considered in the design of vehicle structural strength.

Stress analysis of the carbody revealed that crosswind effects elevated stress concentrations at window

connections by 33.4%. Stress amplitude values after the tunnel exit exhibited a strong correlation with crosswind speed. Higher wind speeds led to greater contributions of aerodynamic loads to the carbody, especially when exiting the tunnel. Higher crosswind speeds resulted in higher dynamic stress peaks, suggesting that safety margins may be exceeded under extreme crosswind conditions. Future research should combine the Goodman correction model to evaluate fatigue life under these conditions and further elucidate the mechanisms of interaction between wind and structural dynamics.

We propose two strategies to reduce aerodynamic stress on high-speed train carbodies: optimizing aluminum alloy structural design at stress-critical zones to lower peak stress and installing roof-mounted vortex baffles to disrupt crosswind–tunnel coupling via interference mechanisms. Combined, these materials and aerodynamic enhancements mitigate risks efficiently, advancing next-generation reliability of carbodies in harsh wind environments.

Acknowledgments

This work is supported by the National Natural Science Foundation of China (No. 52375160) and the Natural Science Foundation of Hebei Province (No. 2024105064), China.

Author contributions

Beikun WANG designed the research and wrote the first draft of the manuscript. Da FENG and Xian CHUAN processed the corresponding data. Yueheng XIANYU helped to organize the manuscript. Yaohui LU revised and edited the final version.

Conflict of interest

Beikun WANG, Yaohui LU, Da FENG, Xian CHUAN, and Yueheng XIANYU declare that they have no conflict of interest.

References

Baker CJ, 2014. A review of train aerodynamics. Part 1–fundamentals. *Aeronautical Journal*, 118(1201):201-228. https://doi.org/10.1017/S000192400000909X

CEN (European Committee for Standardization), 2010. Railway Applications–Structural Requirements of Railway Vehicle Bodies–Part 1: Locomotives and Personal Rolling Stock (and Alternative Method for Freight Wagons), EN 12663-1:2010. CEN, Brussels, Belgium.

CEN (European Committee for Standardization), 2018. Railway Applications–Aerodynamics–Part 6: Requirements and Test Procedures for Cross Wind Assessment, EN 14067-6:2018. CEN, Brussels, Belgium.

CR (China Railway Corporation), 2014. Technical Management Regulations for Railways. China Railway Publishing House, Beijing, China (in Chinese).

Cui T, Zhang WH, 2011. Fluid-solid coupling vibration of train passing through platform at high speed in cross wind. *Journal of Southwest Jiaotong University*, 46(3): 404-408 (in Chinese).

Deng E, Yang WC, He XH, et al., 2020. Transient aerodynamic performance of high-speed trains when passing through an infrastructure consisting of tunnel–bridge–tunnel under crosswind. *Tunnelling and Underground Space Technology*, 102:103440. https://doi.org/10.1016/j.tust.2020.103440

Deng E, Liu XY, Yue H, et al., 2023. How do dunes along a desert urban motorway affect the driving safety of sedans? Evidences from long- and short-term monitoring and IDDES. *Journal of Wind Engineering and Industrial Aerodynamics*, 243:105595. https://doi.org/10.1016/j.jweia.2023.105595

Dou WY, Zhang LL, Chen G, et al., 2019. A combined radial basis function based interpolation method for fluid-structure interaction problems and its application on high-speed trains. *Advances in Engineering Software*, 131:143-152. https://doi.org/10.1016/j.advengsoft.2018.12.006

Hu YL, Ge X, Ling L, et al., 2025. Dynamic performance of a high-speed train exiting a tunnel under crosswinds. *Journal of Zhejiang University-SCIENCE A*, 26(1):21-35. https://doi.org/10.1631/jzus.A2300610

Jing L, Liu K, Ren M, 2019. The transient response of car body and side windows for high-speed trains passing by each other in a tunnel. *Composites Part B: Engineering*, 166:284-297. https://doi.org/10.1016/j.compositesb.2018.11.144

Liu L, Jing L, Li T, et al., 2024. Effects of high geotemperature and high altitude on the pressure wave of high-speed trains running in a long tunnel. *Journal of Zhejiang University-SCIENCE A*, 25(11):953-969. https://doi.org/10.1631/jzus.A2300361

Liu TH, Jiang ZH, Chen XD, et al., 2019. Wave effects in a realistic tunnel induced by the passage of high-speed trains. *Tunnelling and Underground Space Technology*, 86:224-235. https://doi.org/10.1016/j.tust.2019.01.023

Liu TH, Wang L, Li L, et al., 2021. Pressure waves acting on wall of a tunnel and their impact on the tunnel's structural safety. *Journal of Central South University*, 28(10):3223-3237. https://doi.org/10.1007/s11771-021-4823-6

Liu W, Guo DL, Zhang ZJ, et al., 2020. Study of dynamic characteristics in wake flow of high-speed train based on POD. *Journal of the China Railway Society*, 42(9):49-57 (in Chinese). https://doi.org/10.3969/j.issn.1001-8360.2020.09.007

Lu YH, Zhang DW, Zheng HY, et al., 2019. Analysis of the

aerodynamic pressure effect on the fatigue strength of the carbody of high-speed trains passing by each other in a tunnel. *Proceedings of the Institution of Mechanical Engineers, Part F: Journal of Rail and Rapid Transit*, 233(8):783-801. https://doi.org/10.1177/0954409718809469

Miyachi T, Iida M, Fukuda T, et al., 2016. Nondimensional maximum pressure gradient of tunnel compression waves generated by offset running axisymmetric trains. *Journal of Wind Engineering and Industrial Aerodynamics*, 157:23-35. https://doi.org/10.1016/j.jweia.2016.07.015

Mohebbi M, Ma Y, Mohebbi R, 2024. The analysis of utilizing multiple fences in high-speed tracks on the aerodynamic characteristics of a high-speed train model. *Iranian Journal of Science and Technology, Transactions of Mechanical Engineering*, 48(3):847-863. https://doi.org/10.1007/s40997-023-00702-5

Niu JQ, Zhang YC, Li R, et al., 2022. Aerodynamic simulation of effects of one- and two-side windbreak walls on a moving train running on a double track railway line subjected to strong crosswind. *Journal of Wind Engineering and Industrial Aerodynamics*, 221:104912. https://doi.org/10.1016/j.jweia.2022.104912

Niu JQ, Lv DZ, Li R, et al., 2023. Matching of multiple aerodynamic parameters for railway train/tunnel systems to ensure critical airtightness performance of high-speed trains. *Structural and Multidisciplinary Optimization*, 66(1):4. https://doi.org/10.1007/s00158-022-03462-z

Tang JW, Xu GF, Zhang JY, et al., 2024. Influence of lift wings on aerodynamic characteristics and operation safety of trains. *Journal of Transportation Engineering and Information*, 22(2):173-190 (in Chinese). https://doi.org/10.19961/j.cnki.1672-4747.2023.09.014

NRA (National Railway Administration of the People's Republic of China), 2019. Strength Design and Test Accreditation Specification for Roiling Stock-Car Body–Part 1: Passenger Car Bodies, TB/T 3550.1-2019. Railway Industry Standard of the People's Republic of China.

Wang B, Xu J, 2023. Application of different sub-grid models used in large-eddy simulation of flow around a cylinder at *Re*=3900. *Experimental Techniques*, 47(1):187-195. https://doi.org/10.1007/s40799-022-00568-3

Wang BK, Feng D, Lu YH, et al., 2025. Effect analysis of high-speed trains passing by each other in tunnel on its vibration characteristics. *Journal of Railway Science and Engineering*, 22(3):930-941 (in Chinese).

Wang J, Deng E, Ni YQ, et al., 2024. Mitigating inflow acceleration effects in twin mountains using air jets: emphasis on anti-wind for high-speed railways. *Physics of Fluids*, 36(5):055128. https://doi.org/10.1063/5.0202419

Wang L, Luo JJ, Li FL, et al., 2021. Aerodynamic performance and flow evolution of a high-speed train exiting a tunnel with crosswinds. *Journal of Wind Engineering and Industrial Aerodynamics*, 218:104786. https://doi.org/10.1016/j.jweia.2021.104786

Wang L, Luo JJ, Li FL, 2022. Transient pressure and train wind during high-speed train entering a tunnel under crosswind. *Journal of Vibration and Shock*, 41(3):27-36 (in Chinese). https://doi.org/10.13465/j.cnki.jvs.2022.03.004

Xia C, Shan XZ, Yang ZG, 2017. Comparison of different ground simulation systems on the flow around a high-speed train. *Proceedings of the Institution of Mechanical Engineers, Part F: Journal of Rail and Rapid Transit*, 231(2):135-147. https://doi.org/10.1177/0954409715626191

Zheng ZW, Yi C, Liao XK, 2024. Research on the influence of line conditions on the load characteristics of axle box bearing of high-speed train. *Journal of Mechanical Engineering*, 60(20):251-260 (in Chinese). https://doi.org/10.3901/JME.2024.20.251

Zhou D, Xia CJ, Wu LL, et al., 2023. Effect of the wind speed on aerodynamic behaviours during the acceleration of a high-speed train under crosswinds. *Journal of Wind Engineering and Industrial Aerodynamics*, 232:105287. https://doi.org/10.1016/j.jweia.2022.105287

Zhou P, Zhang JY, Li T, et al., 2019. Numerical study on wave phenomena produced by the super high-speed evacuated tube maglev train. *Journal of Wind Engineering and Industrial Aerodynamics*, 190:61-70. https://doi.org/10.1016/j.jweia.2019.04.003

Electronic supplementary materials

Sections S1–S11